The El Niño event of 2015-16: Climate anomalies and their impact on groundwater resources in East and Southern Africa

S.R. Kolusu[1], M. Shamsudduha[2,3], M.C. Todd[1], R.G. Taylor[3], D. Seddon[3], J. J. Kashaigili[4], G.Y. Ebrahim[5], M. Cuthbert[3,6], J.P.R. Sorensen[7], K.G. Villholth[5], A.M. MacDonald[8], and D.A. MacLeod[9]

1. Department of Geography, University of Sussex, Brighton, BN1 9QS, UK s.kolusu@sussex.ac.uk
2. Institute for Risk and Disaster Reduction, University College London, Gower Street, London WC1E 6BT, UK
3. Department of Geography, UCL, Gower Street, London WC1E 6BT UK
4. Sokoine University of Agriculture, Morogoro, Tanzania
5. International Water Management Institute, Pretoria, South Africa
6. School of Earth and Ocean Sciences, Cardiff University, Main Building, Park Place, Cardiff, CF10 3AT, UK
7. British Geological Survey, Maclean Building, Crowmarsh Gifford, Wallingford, Oxfordshire OX10 8BB UK
8. British Geological Survey, The Lyell Centre, Research Avenue South, Edinburgh EH14 4AP UK
9. Oxford University, Atmospheric, Oceanic and Planetary Physics, UK

Keywords

El Nino; ENSO; Climate; groundwater; Africa; sustainability; recharge; climate impacts; water management; GRACE

Supplementary Information

S1. Climatological context: El Niño and other drivers of climate over EASE/SA, the 2015-16 El Niño event and climate anomalies over SA

The climatological mean austral summer wet season of October-April rainfall (figure S1(a)) shows a maximum extending Northwest-Southeast from Democratic Republic of Congo (DRC)/Angola in the west, across Zambia, Malawi to northern Mozambique in the East. The leading mode of interannual variability in rainfall and SPEI-7, is a north/south dipole pattern of opposing anomalies across EASE and SA, with a divide at $\sim 11^{o}$S, the approximate mean latitude of rainfall maximum and is strongly related to ENSO. This structure clearly evidenced by the leading Empirical Orthogonal Function (EOF) of SPEI-7 (figure S1(b)) which explains 21.5% of total variance. The time coefficients correlate strongly with tropical SSTs (figure S1(d)) highly characteristic of the ENSO SST anomalies in both the Pacific and Indian Oceans, notably the SW/NE positive/negative correlation dipole across the southwest/equatorial Indian Ocean (e.g. Lindesay, 1988; Reason *et al.*, 2000, Lazenby *et al.*, 2016). As such, for Africa South of the equator the leading mode of climate variability is strongly related to ENSO, with wet (dry) anomalies during El Niño (la Niña) events across EASE (SA). The EOF pattern is largely insensitive to the length of choice of months in the wet season. This north-south dipole response across EASE/SA to ENSO has been well documented previously (Ropelewski and Halpert, 1987; Janowiak, 1988; Goddard and Graham, 1999; Manatsa *et al.*, 2011), although the physical mechanisms of teleconnection remain elusive (see Blamey *et al.* 2018 for a summary).

The climate anomaly pattern during 2015-16 was highly characteristic of this mode (compare figures 1(a) and S1b). Very strong SST anomalies over the Pacific and elsewhere in the tropics during 2015-16 (figure S1(d)) were associated with a strong north/south dipole in rainfall with drought in SA (figure 1(a)). The socio-economic impacts were pronounced, with much of SA affected by drought, leading to a regional drought disaster declaration by the Southern Africa Development Community (SADC). By September 2016, six SADC countries had declared 'national drought emergencies' (Botswana, Namibia Lesotho, Malawi, Swaziland and Zimbabwe) with drought emergency declared for seven of the South Africa's nine provinces, and a temporary red alert also declared for central and Southern provinces of Mozambique (SADC 2016a). The drought resulted in an extensive loss of crops and livestock, an increase in food prices, driving an estimated 39 million people into deeper food insecurity (SADC 2016a; 2016b; Archer *et al.*, 2017). Surface water shortages further affected electricity generation and domestic supply, affecting economic activity and human health (SADC, 2016a; Siderius *et al.* 2018).

The 2015-16 El Niño was without doubt one of the strongest on record, and by some indicators was actually the strongest. There are many measures of ENSO strength (see e.g. https://www.esrl.noaa.gov/psd/enso/dashboard.html), which provide a mixed picture on the relative strength of the major events. 2015-16 appears strongest based on the Niño 3.4, Niño 4 and Bivariate El Niño – Southern Oscillation index, whilst 1997-98 is the strongest based on the (East pacific Niño 3 and 1+2 SST indices, east Pacific heat content and the Multivariate El Niño index. However, 2015-16 was certainly more persistent that 1997-98 with many indices turning positive at some time in 2014 related to the El Nino event that was predicted in 2014 but did not develop fully until 2015-16 (Levine and McPhaden, 2016).

However, there is substantial diversity in the character of El Niño events, in terms of both (i) the structure and magnitude of anomalies in the Pacific sector. For example, 2015-16 and 1997-98 differed in that the former was stronger in the Central Pacific sector (Niño3.4 and Niño SST region) and the latter in the East Pacific (Niño 1+2 and Niño 3 SST regions) (ii) the state and evolution of other regional drivers of climate variability which interact with ENSO teleconnection processes, such that the remote impacts over Africa can be quite variable (e.g. Ratnam *et al.,* 2014; Preethi *et al.*, 2015,;Hoell *et al.,* 2017; Blamey *et al.,* 2018). Across Southern Africa (SA) multiple regional structures of ocean and atmospheric variability modulate the impacts of ENSO including the South Indian Ocean dipole (Reason, 2001) as well as the Angola low and Botswana High atmospheric features (Blamey *et al.,* 2018). Furthermore, intraseasonal variability associated with the Madden Julian Oscillation, with 30-60 day timescales can also modulate interannual drivers of variability, particularly over East Africa (Berhane and Zaitchik, 2014).

Over East Africa rainfall is more strongly related to the state of the Indian Ocean than to ENSO. The Indian Ocean Zonal mode (IOZM), an east-west pattern of atmosphere-ocean variability across the Equatorial Indian ocean, strongly modulates the regional Walker circulation and hence rainfall over East Africa. During positive IOZM events warmer ocean temperatures in the equatorial west Indian Ocean and cooler temperatures in the east lead to enhanced rainfall over EASE, with negative IOZM leading to a reduction in rainfall (see Nicholson 2017 for a review and references therein). The impact of ENSO on EASE is therefore intimately connected to the state of the IOZM (Black *et al.,* 2003, Manatsa *et al.,* 2011). During 2015-16 the IOZM was only weakly positive (see SST anomalies in figure S1(d)) and the seasonal de-trended IOZM index (Saji *et al.,* 1999) in 2015-16 was ranked 16^{th} out of 150 years. As a result, the mean equatorial zonal Indian Ocean Walker cell with ascent (descent) in the east at ~100^{o}E (west at ~50^{o}E) of the basin is only weakly perturbed. The zonal cross section over the East Africa-Indian Ocean sector indicates that enhanced large-scale uplift is limited to a quite restricted region of EASE from ~33^{o}-40^{o}E. In this way, the weak reorganisation of the Indian ocean Walker circulation led to rather moderate rainfall anomalies over EASA (Section 3.1).

S2. The Standardised Precipitation-Evapotranspiration Index (SPEI) and other data used

We derive the 7-month SPEI October-April (Vincente-Serrano *et al.,* 2010) over the period 1901 to present, using precipitation data from the Global Precipitation Climatology Centre (GPCC) monthly product v7 (Schneider *et al.*, 2011a; Schneider *et al.*, 2013) at 1.0° resolution, extended beyond 2013 by combining with the GPCC V4 monitoring product (Schneider *et al* 2011b). To account for uncertainty in estimation of PET we use three parameterisations of varying complexity: The Penman-Montieth equation, based on net radiation, temperature, wind-speed and vapour pressure); The Hargreaves equation, based on mean, minimum and maximum temperature and extra-terrestrial solar radiation; The Thornthwaite equation, which is based solely on surface air temperature. The variables required for the various PET estimates are obtained from the CRUTS3.24.01 dataset (Harris *et al.,* 2014).

There is evidence to indicate recharge is preferentially driven by intense rainfall (see references in Sections 1 and 3.1.1). To examine the impact of El Niño on rainfall intensities within the Oct-April 2015-16 season we use derive percentiles of the daily rainfall probability distribution from the TRMM3B42 product. In the absence of robust knowledge of actual rainfall thresholds associated with groundwater recharge, and the likelihood that such thresholds are highly variable in space and time, we use the 80th percentile of daily rainfall within the season as a coarse proxy for rainfall events likely to be associated with recharge. Our results (Section 3.1.1 are largely insensitive to the choice of percentile value (not shown). Information on the large-scale atmospheric circulation is diagnosed from the horizontal and vertical winds, and specific humidity from ERA-Interim reanalysis data (Dee *et al.,* 2011). SST data are obtained from the extended reconstructed sea surface temperature (ERSST) version 4 from the National Oceanographic and Atmospheric Administration (NOAA) (Smith *et al* 2008) on a 2° grid.

<u>S3. SPEI-7 Intensity-Area-Frequency (IAF) curves and associated return period estimates, and attribution of anthropogenic influence</u>

Droughts are spatially extensive but variable features. We represent the spatial extent using IAF curves which show the intensity of SPEI-7 water balance anomalies across all spatial scales within a study domain. IAF curves are independent of the precise spatial patterns of SPEI-7 anomalies, and as such allow us to compare droughts between individual years, and to calculate the return periods for drought events across scales. This direct comparability of SPEI-7 IAF curves is valuable since no two drought events have exactly the same spatial pattern. The IAF curves are derived using the method of Mishra and Cherkauer (2010) separately over the two study domains of EASE and SA, by calculating the mean SPEI-7 value of grid cells lying within various areal extent intervals: The areas covered by the lowest (for SA) or highest (for EASE) 5th, 10th, 20th…100th areal percentiles of SPEI grid cell values within the domain area i.e. when all grid cells are ranked. This allows, for each season, the mean SPEI-7 IAF curve to be plotted (see figure 3).

We then estimate the return period of the 2015-16 El Niño event by comparing the observed SPEI-7 IAF curve of 2015-16 with IAF curves representing various 'benchmark' return periods (figure 3) and finding the closest match, by least squared error. Estimating these benchmark return periods of drought events is challenging given the relatively short observational record for what are relatively long duration events, and indeed because of non-stationarity in climate records under a changing climate. We address both these challenges in our approach. To counter the problem of insufficient sampling of the extreme tail of the distribution, we increase our sample of climate events beyond the observed record using large ensembles of climate model simulations from the HAPPI experiment (Mitchell *et al.,* 2017). HAPPI is designed specifically to quantify climate extremes, through the use of relatively high model resolution and large initial-condition ensembles. We use precipitation data from four atmospheric models, namely HadGEM3, CAM5, MIROC5 and NorESM, (degraded to common resolution of 1^{o}) each with 10 ensemble members, run over the period ~1950s-2010s, forced with observed SSTs and 'historical' greenhouse gases and aerosol radiative forcings. These simulations provide about 2400 years of simulated data, with greater statistical definition of the extreme tail of the distribution required for the extreme events, notably the 2015-16 drought over SA which is the strongest on record. As with the observations we derive the mean SPEI-7 for each areal extent interval (5th, 10th, etc. spatial percentiles over the domain), for each of the ~2400 model years. Estimation of return periods is based on the Extreme Value Theory (EVT), widely used for the description of rare climate events in the extreme tail of the parameter distribution. The Generalized Extreme Value distribution (GEV) is fitted to the distribution of only the extreme SPEI-7 values, for each areal extent separately (using maximum likelihood estimation and a chi-squared goodness-of-fit test, Coles et al., 2001). This distribution of extremes ('block maxima') is composed of the most intense SPEI-7 values (for drought over the SA domain SPEI-7 is multiplied by -1) within non-overlapping 'blocks' of 30 years, a standard climatological period. Then, return periods are estimated by inverting the resulting GEV cumulative probability distribution for a range of periods from 30-300 years, for each areal extent separately, providing IAF curves for benchmark return periods (see figure 3). Whilst our approach is similar to previous drought analyses (e.g. Robeson, 2015) we recognise a number of caveats. First, the estimated return periods are sensitive to the arbitrary choice of block size and we estimate the uncertainty associated with this using periods of 25-60 years. Second, whilst the large ensembles provided by the HAPPI experiment are designed specifically for analysis of extremes they necessarily provide only a partial representation of the climate variability 'space'.

For estimation of return periods shorten than the duration of one 'block' (30 years), we follow Mishra and Cherkauer (2010) and Philip *et al.* (2018) in fitting a distribution to the historical record of SPEI-7 data. For each areal extent interval (5th, 10th, etc. spatial percentiles) we fit a GEV distribution to the 116 historical SPEI-7 data points. We then invert the cumulative distribution to derive return periods for every spatial percentile, giving a set of IAF benchmark return period curves. Finally, we conduct all the above IAF curve return period analysis using SPEI-7 derived with each of the three PET equations and provide the average return period estimates and the associated range to represent this component of uncertainty.

It is likely that anthropogenic climate change is, and will continue to, affect large-scale hydrology. As such, climate risks are changing and non-stationarity in climate records complicates the interpretation of return periods. However, the IPCC recent assessment report concludes that there is only low confidence in detection and attribution of observed changes in drought extremes globally (Bindoff *et al.*, 2013), largely due to uncertainties in distinguishing relatively small trends in precipitation from decadal variability, especially given limitations in precipitation data. Nevertheless, attribution of recent temperature rises is robust even down to the regional/continental scale (Bindoff *et al.*, 2013). In recent probabilistic event attribution analyses of tropical drought events the contribution of anthropogenic temperature effects is discernible, in contrast to that of precipitation (Marthews *et al.*, 2015). As such, the full causal chain from climate anomaly through water balance to agricultural drought is complex and typically not well represented in models such that attribution of drought remains extremely challenging. Therefore, here we estimate the effects purely of anthropogenic temperature trends on drought risk over SA through a simplified attribution experiment. The SPEI-7 IAF return period analysis above is repeated, but in deriving the benchmark return period curves the temperature data, used in calculating PET, has the signal of anthropogenic climate change removed. Specifically, PET is estimated using the HAPPI multi-ensemble mean temperature from a counterfactual world without human influence on radiative forcing: the ‘natural’ runs, in which only the natural forcings (solar variability and volcanic aerosols) are provided to the models. To ensure space-time consistency in all the climate variables whilst changing the temperature data, we used the 30-year smoothed temperature from the ‘natural’ model runs to which is added the anomalies of temperature from the ‘historical’ run with respect to a 30-year running mean. Not that we derive the SPEI-7 over both datasets merged together so that the effect of the temperature perturbation between the ‘natural’ and ‘historical’ runs is reflected in the resulting SPEI-7 values, given that the index is standardised across the timeseries. The benchmark return period IAF curves are then derived from the SPEI-7 values for each dataset separately. Thus, comparing the estimated SPEI-7 IAF return periods from the climate with 'historical' temperature with those from a counterfactual climate with the 'natural' only temperature, provides an indication of the influence of the anthropogenic temperature trend effects on drought risk over SA. We note that the SPEI is quite temperature dependent through PET calculation such that other drought indices may yield different sensitivity to warming.

We must emphasise that this analysis deliberately considers only the effects of the slowly evolving anthropogenic influence on temperature. We do not consider anthropogenic influences on rainfall and the other determinants of PET i.e. wind speed, humidity, radiation budget, no any changes to variability in temperature. As such, in utilising a large model ensemble to define the statistics of extreme events, we retain some features of the probabilistic event attribution method (e.g. Allen et al., 2003, Stott et al., 2014) but focus solely on that aspect of climate change (near surface temperatures) for which we have greatest confidence in the ability of models to represent with credibility.

S4 Groundwater storage estimates from GRACE and LSMs

To address uncertainty associated with different GRACE processing strategies to resolve ΔTWS (Eq. 1) we apply an ensemble mean of three GRACE TWS. Namely, the CSR land (version RL05.DSTvSCS1409, Swenson and Wahr, 2006; Landerer and Swenson ,2012) and JPL Global Mascon (version RL05M_1.MSCNv01, Watkins *et al.*, 2015; Wiese *et al.*, 2015) solutions, from NASA's *GRCTellus* data dissemination site (http://grace.jpl.nasa.gov/data), and a third GRGS GRACE solution (CNES/GRGS release RL03-v1) (Biancale *et al.,* 2006) from the French Government space agency, Centre National D'études Spatiales (CNES).

GRCTellus CSR land solution (version RL05.DSTvSCS1409) is post-processed from spherical harmonics released by the Centre for Space Research (CSR) at the University of Texas at Austin. *GRCTellus* gridded datasets are available at a monthly time step and a spatial resolution of 1° × 1° (~111 km at equator) though the actual spatial resolution of GRACE footprint is ~450 km or ~200,000 km^2 (Scanlon *et al.,* 2012). To amplify TWS signals we apply the dimensionless scaling factors provided as 1° × 1° bins that are derived from minimising differences between TWS estimated from GRACE and the hydrological fields from the Community Land Model (CLM4.0) (Landerer and Swenson, 2012). JPL-Mascons (version RL05M_1.MSCNv01) data processing involves the same glacial isostatic adjustment correction but applies no spatial filtering as JPL-RL05M directly relates inter-satellite range-rate data to mass concentration blocks (mascons) to estimate monthly gravity fields in terms of equal area 3° × 3° mass concentration functions in order to minimise measurement errors. Gridded mascon fields are provided at a spatial sampling of 0.5° in both latitude and longitude (~56 km at the equator). Similar to *GRCTellus* CSR product, dimensionless scaling factors are provided as 0.5° × 0.5° bins (Shamsudduha *et al.*, 2017) that also derive from the Community Land Model (CLM4.0) (Wiese *et al.*, 2016). The scaling factors are multiplicative coefficients that minimize the difference between the smoothed and unfiltered monthly ΔTWS variations from the CLM4.0 hydrology model (Wiese *et al.*, 2016). GRGS monthly GRACE products (version RL03-v1) are processed and made publicly available (http://grgs.obs-mip.fr/grace) by CNES (Shamsudduha *et al.*, 2017). Further details on the Earth's mean gravity-field models can be found on the CNES official website of GRGS/LAGEOS (http://grgs.obs-mip.fr/grace/).

GRACE ΔTWS time-series data have some missing records as the satellites are switched off for conserving battery life (Shamsudduha *et al.*, 2017); these missing records are linearly interpolated (Shamsudduha *et al.*, 2012). Monthly ΔTWS time-series data as equivalent water depth (cm) are extracted from GRACE TWS datasets by creating a 200 km radial buffer (i.e. area equivalent of ~120 000 km^2) around at two groundwater-level monitoring sites (Makutapora and Limpopo) and by the point of interest and taking the mean values aggregating the selected grid points.

To derive ΔGWS from GRACE ΔTWS (eq. 1), we use simulated soil moisture to represent ΔSMS and surface runoff, as a proxy for ΔSWS (Mishra *et al.*, 2016), from LSMs within NASA's Global Land Data Assimilation System (GLDAS). GLDAS is an uncoupled land surface modelling system that includes multiple global LSMs driven by surface meteorology from the NCEP data assimilation system, CMAP disaggregated precipitation and the Air Force Weather Agency satellite-derived radiation fields (Rodell *et al.*, 2004). We apply monthly ΔSMS and surface runoff data at a spatial resolution of 1° × 1° from 4 GLDAS LSMs: The Community Land Model (CLM, version 2) (Dai *et al.*, 2003), NOAH (version 2.7.1) (Ek *et al.*, 2003), the Variable Infiltration Capacity (VIC) model (version 1.0) (Liang *et al.*, 2003), and MOSAIC Mosaic (version 1.0) (Koster and Suarez, 1992). The respective total depths of modelled soil profiles are 3.4 m, 2.0 m, and 1.9 m and 3.5 m in CLM (10 vertical layers), NOAH (4 vertical layers), and VIC (3 vertical layers), and Mosaic (3 vertical layers) (Rodell *et al.*, 2004). In the absence of in situ ΔSMS and ΔSWS data in the study areas, we apply an ensemble mean of the 4 LSMs-derived ΔSMS and ΔSWS data in order to disaggregate GRACE ΔTWS signals across our study regions, for the period August 2002 to July 2016, similar to the approach applied for other locations by Shamsudduha *et al.* (2012; 2017). To help interpretation of these mean ΔGWS signals we also present the total uncertainty in estimates of ΔGWS which result from the uncertainty in estimates of ΔTWS, ΔSMS and ΔSWS (blue shading in figure 5(c)). The uncertainty in these individual water balance components is shown in figure S2 i.e. the range in estimated GRACE ΔTWS across the three retrieval estimates, and the ranges in estimates ΔSMS and ΔSWS across the four LSMs. Overall, the total uncertainty in ΔGWS can be substantial and receives roughly equal contribution from uncertainty in ΔTWS and ΔSMS with uncertainty in ΔSWS important only occasionally. There is some indication that during the periods of greatest ΔGWS uncertainty, the ΔTWS uncertainty is most important e.g. 2009-10 and 2015-16 at Limpopo. For further understanding of the uncertainty in the estimates water storage from LSMs with respect to GRACE readers are referred to Scanlon et al. (2018).

S5. Groundwater storage estimates from piezometric observations

Groundwater-level time series records were compiled in two areas situated at the heart of the two EASE/SA ENSO rainfall dipole centres of action (figure 1(a)). (i) The Makutapora wellfield (35.75°E, 5.90°S) site in central Tanzania, East Africa. Groundwater records were collated from the Ministry of Water and Irrigation and the Dodoma Urban Water Supply, Tanzania. Here, groundwater is abstracted from an aquifer comprising deeply weathered granite overlain by alluvium (*Taylor et al.*, 2013). Data from three sites in the wellfield met the data quality criteria and are averaged together; mean groundwater-level time series records were converted to monthly anomalies in GWS using an in-situ derived S_y value of 0.06 (*Taylor et al.*, 2013). We estimate that these data are representative of groundwater levels across an area of ~60 km^2 (Taylor *et al.*, 2013). (ii) Limpopo Basin in Southern Africa (~28 to 32°E, 22.5 to 25°S). Groundwater-level records from 40 stations within weathered hard-rock ("basement") aquifers in sub-basins A6 (Mogalakwena), A7 (Sand), A8 (Nzhelele) and A9 (Luvuvhu) of the Limpopo Basin were collated from the Department of Water and Sanitation, Directorate Surface and Groundwater Information, South Africa. The data were first standardised then averaged together and represent an area estimated to be ~ 47 000 km^2. For both sites daily to monthly groundwater-level records within our common study period of August 2002 to July 2016, were checked for consistency (missing data less than 10%) and selected for groundwater storage analysis. Mean groundwater-level time series records were converted to monthly anomalies in GWS using a S_y value that produced the lowest root-mean square error between in situ and GRACE GWS; the applied value (0.025) is consistent with that estimated for basement aquifers in Africa by MacDonald *et al.* (2012).

We acknowledge that our estimates of GWS from piezometry may be influenced by abstractions and we provide data on pumping rates from Makutapora (figure 5(c)). A numerical method to remove the effects of pumping is currently the subject of ongoing research by the authors, so in this case we infer the effect of pumping on GWS only in only relative qualitative terms. Equivalent direct data on direct pumping rates is not available at Limpopo. However, we note that Cai *et al.* (2017) mapped the spatial extent of irrigation across the Limpopo basin in South African using satellite data and estimated that irrigation from groundwater provides about 50% of the irrigated areas over 2% of the land area, which likely influences groundwater storage locally.

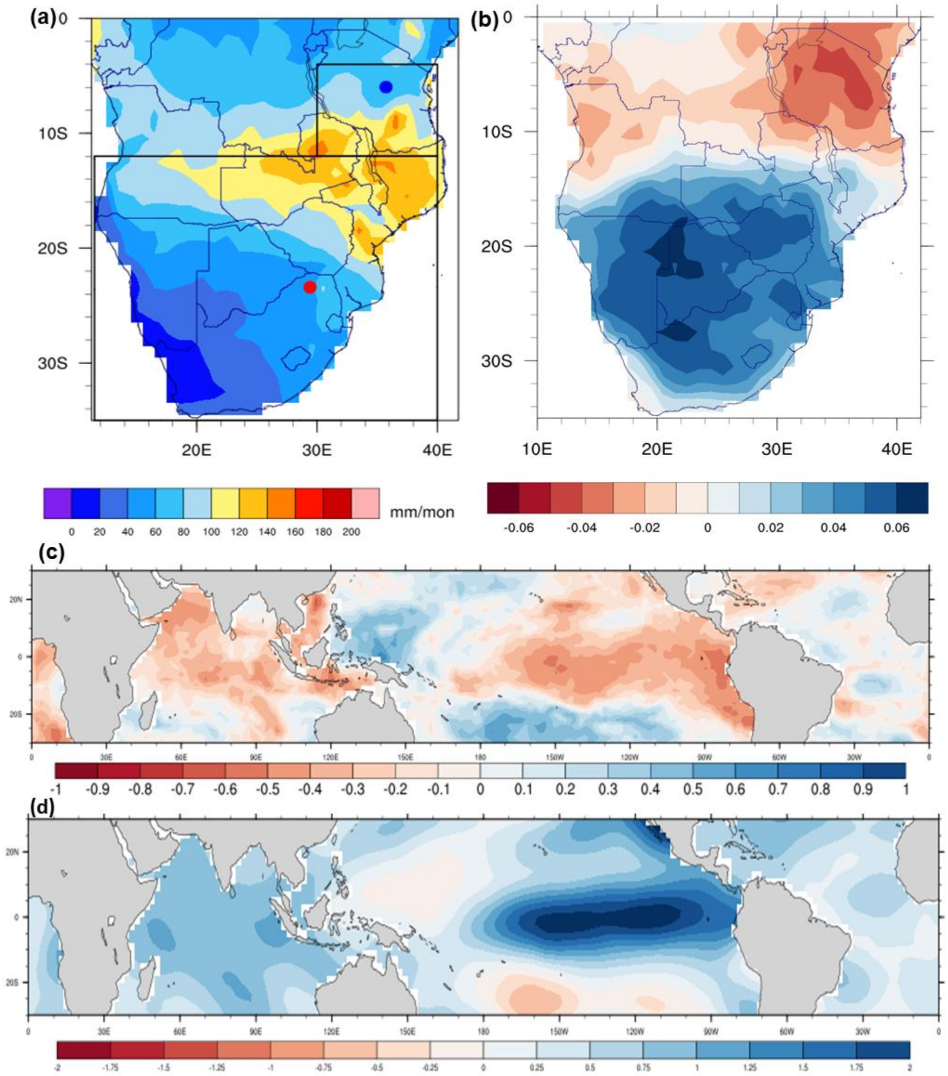

Figure S1. (a) Climatological precipitation for the October-April season for the period of 1901-2016 (mm month^{-1}). Boxes in figure S1(a) show the EASE (small box) and SA (big box) domains used in the IAF analysis (see Section 2.1). The blue and red filled circles denote the piezometer observation locations at Makutapora, Tanzania and Limpopo, South Africa, respectively. (b) Leading mode of interannual October-April variability calculated using the empirical orthogonal function (EOF) analysis of de-trended rainfall of GPCC. (c) Correlation between coefficients of EOF1 (figure S1(b)) and global SST (October-April mean) 1901-2016. (d) SST anomalies (K) October-April 2015-16

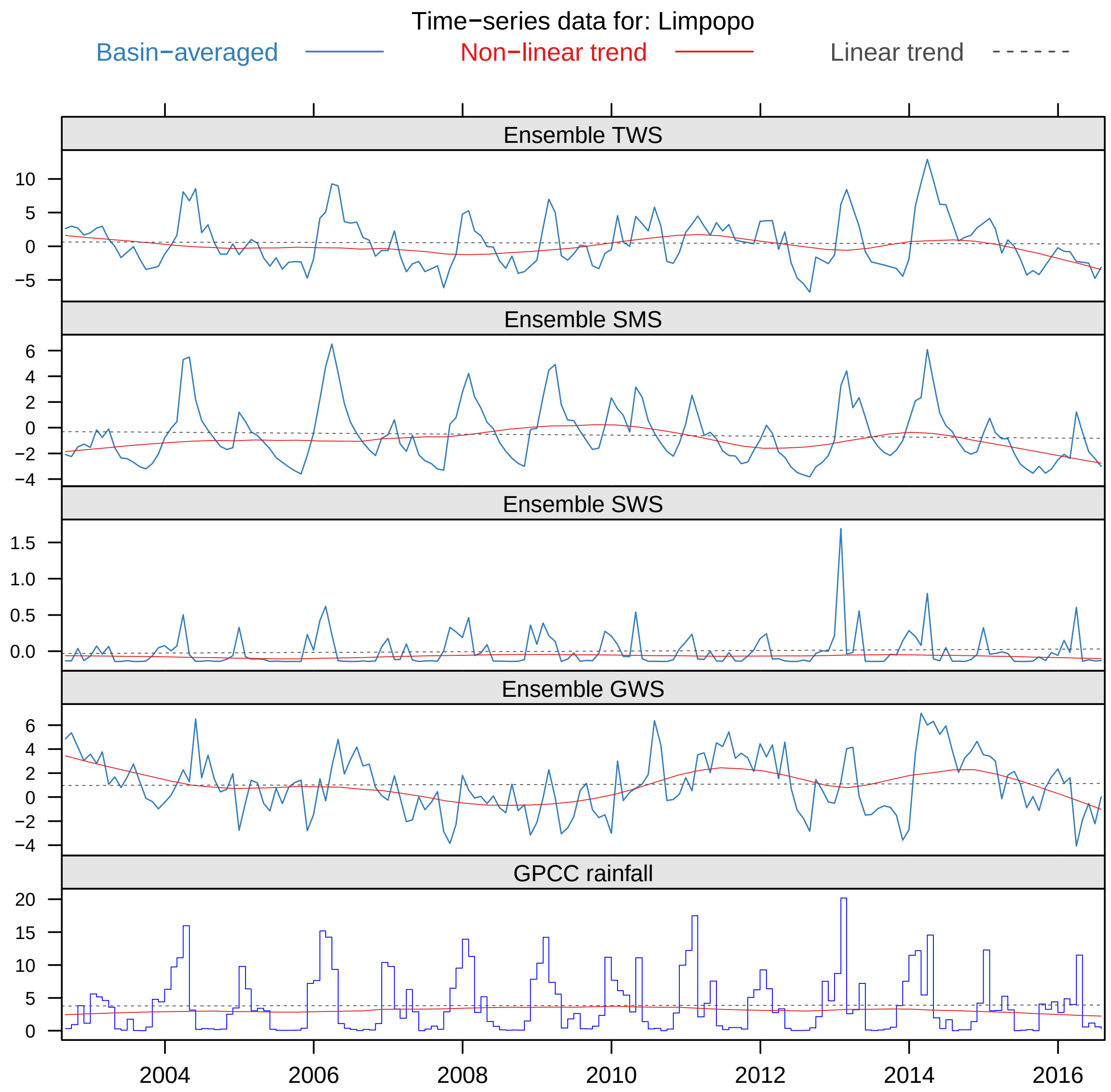
Time−series data for: Limpopo
Basin−averaged
Non−linear trend
Linear trend
Ensemble TWS
Ensemble SMS
Ensemble SWS
Ensemble GWS
GPCC rainfall
2004
2006
2008
2010
2012
2014
2016

349

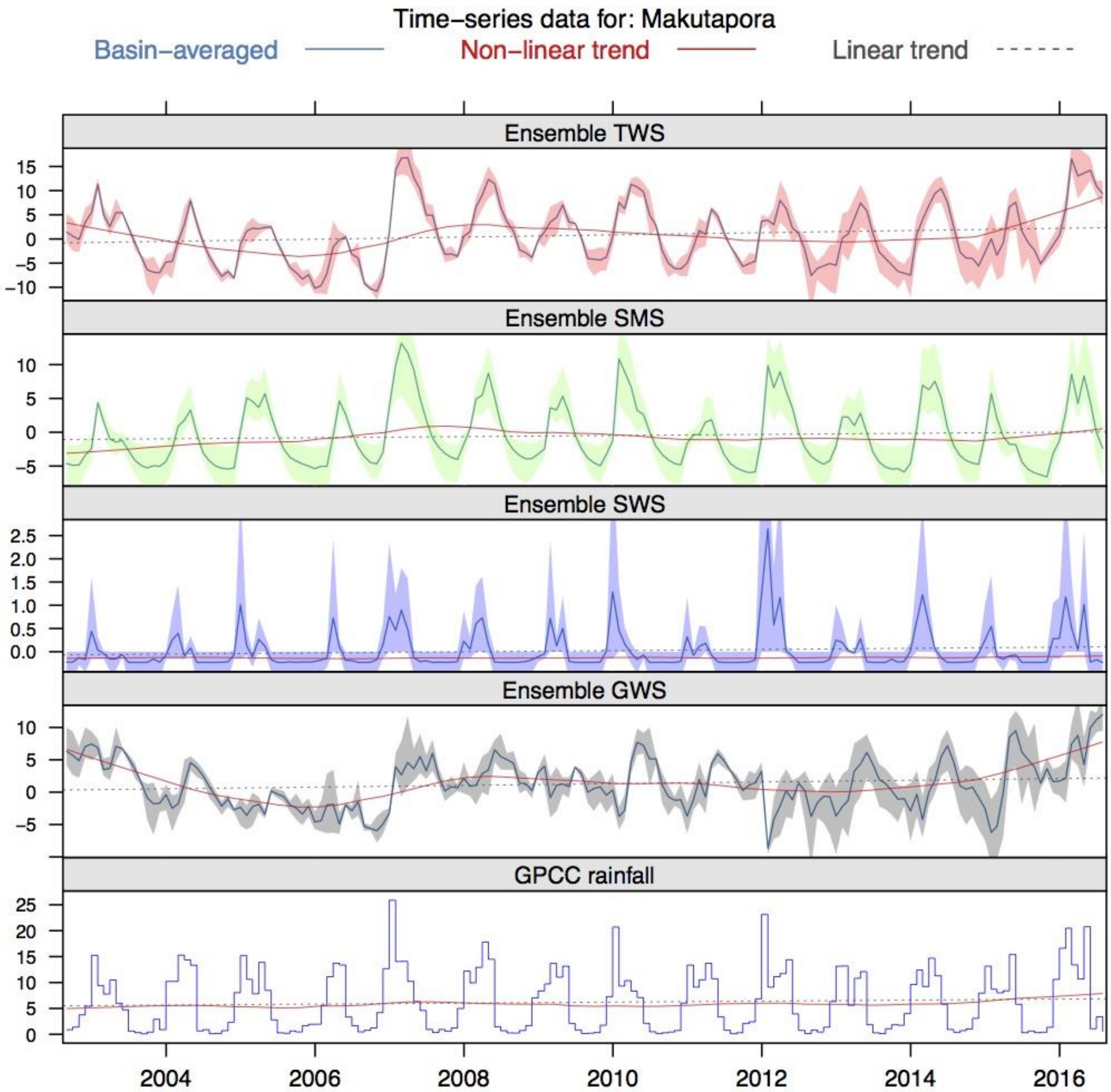

Figure S2: Time series of monthly estimates of anomalies in the individual components of water balance (lines) and the associated uncertainty range (shaded). From top to bottom TWS from GRACE; SMS and SWS both from LSMs; the residual GWS; observed GPCP rainfall, (all in cm) at (a) Limpopo (b) Makutapora.

References.

Allen, M. : Liability for climate change, *Nature*, *421*(6926), 891,2003.

Archer, E. R. M., Landman, W. A., Tadross, M. A., Malherbe, J., Weepener, H., Maluleke, P., & Marumbwa, F. M.: Understanding the evolution of the 2014–2016 summer rainfall seasons in southern Africa: Key lessons, *Climate Risk Management*, *16*, 22-28, 2017.

Bindoff, N.L., P.A. Stott, K.M. AchutaRao, M.R. Allen, N. Gillett, D. Gutzler, K. Hansingo, G. Hegerl, Y. Hu, S. Jain, I.I. Mokhov, J. Overland, J. Perlwitz, R. Sebbari and X. Zhang,: Detection and Attribution of Climate Change: from Global to Regional. In: Climate Change 2013: The Physical Science Basis. Contribution of Working Group I to the Fifth Assessment Report of the Intergovernmental Panel on Climate Change [Stocker, T.F., D. Qin, G.-K. Plattner, M. Tignor, S.K. Allen, J. Boschung, A. Nauels, Y. Xia, V. Bex and P.M. Midgley (eds.)]. Cambridge University Press, Cambridge, United Kingdom and New York, NY, USA,2013.

Berhane, F., & Zaitchik, B: Modulation of daily precipitation over East Africa by the Madden–Julian oscillation, *Journal of Climate*, *27*(15), 6016-6034, 2014.

Biancale, R., Lemoine, J-M., Balmino, G., Loyer, S., Bruisma, S., Perosanz, .F, Marty, J-C., and Gégout, P.: 3 Years of Geoid Variations from GRACE and LAGEOS Data at 10-day Intervals from July 2002 to March 2005, CNES/GRGS, 2006

Black, E., Slingo, J., & Sperber, K. R. :An observational study of the relationship between excessively strong short rains in coastal East Africa and Indian Ocean SST, *Monthly Weather Review*, *131*(1), 74-94, 2003.

Blamey, R. C., Kolusu, S. R., Mahlalela, P., Todd, M. C., & Reason, C. J. C: The role of regional circulation features in regulating El Niño climate impacts over southern Africa: A comparison of the 2015/2016 drought with previous events, *International Journal of Climatology*, **https://doi.org/10.1002/joc.5668**, 2018.

Cai, X., Magidi, J., Nhamo, L., & van Koppen, B.: *Mapping irrigated areas in the Limpopo Province, South Africa*(Vol. 172),International Water Management Institute (IWMI Working Paper 172), doi: 10.5337/2017.205 , 2017.

Coles, S., Bawa, J., Trenner, L., & Dorazio, P.:*An introduction to statistical modelling of extreme values* (Vol. 208), London: Springer, 2001.

Dai, Y., Zeng, X., Dickinson, R. E., Baker, I., Bonan, G. B., Bosilovich, M. G., ... & Oleson, K. W. :The common land model, *Bulletin of the American Meteorological Society*, *84*(8), 1013-1024, 2003.

Dee, D. P., Uppala, S. M., Simmons, A. J., Berrisford, P., Poli, P., Kobayashi, S., ... & Bechtold, P.: The ERA-Interim reanalysis: Configuration and performance of the data assimilation system, *Quarterly Journal of the royal meteorological society*, *137*(656), 553-597, 2011.

Ek, M. B., Mitchell, K. E., Lin, Y., Rogers, E., Grunmann, P., Koren, V., ... & Tarpley, J. D. :Implementation of Noah land surface model advances in the National Centers for Environmental Prediction operational mesoscale Eta model, *Journal of Geophysical Research: Atmospheres*, *108*(D22), 2003.

Goddard, L., & Graham, N. E. :Importance of the Indian Ocean for simulating rainfall anomalies over eastern and southern Africa, *Journal of Geophysical Research: Atmospheres*, *104*(D16), 19099-19116, 1999.

Harris, I. P. D. J., Jones, P. D., Osborn, T. J., & Lister, D. H. :Updated high-resolution grids of monthly climatic observations–the CRU TS3. 10 Dataset, *International journal of climatology*, *34*(3), 623-642, 2014.

Hoell, A., Funk, C., Zinke, J., & Harrison, L. : Modulation of the southern Africa precipitation response to the El Niño Southern Oscillation by the subtropical Indian Ocean dipole, *Climate dynamics*, *48*(7-8), 2529-2540, https://doi.org/10.1007/s00382-016-3220-6,2017.

Janowiak, J. E. :An investigation of interannual rainfall variability in Africa. *Journal of Climate*, *1*(3), 240-255, 1988.

Koster, R. D., & Suarez, M. J. : Modeling the land surface boundary in climate models as a composite of independent vegetation stands, *Journal of Geophysical Research: Atmospheres*, *97*(D3), 2697-2715, 1992.

Landerer, F. W., & Swenson, S. C. :Accuracy of scaled GRACE terrestrial water storage estimates, *Water resources research*, *48*(4), 2012.

Lazenby, M. J., Todd, M. C., & Wang, Y. : Climate model simulation of the South Indian Ocean Convergence Zone: mean state and variability, *Climate Research*, *68*(1), 59-71, 2016.

Liang, X., Xie, Z., & Huang, M. :A new parameterization for surface and groundwater interactions and its impact on water budgets with the variable infiltration capacity (VIC) land surface model, *Journal of Geophysical Research: Atmospheres*, *108*(D16), 2003.

Lindesay, J. A. : South African rainfall, the Southern Oscillation and a Southern Hemisphere semi-annual cycle, *Journal of Climatology*, *8*(1), 17-30, 1988.

Levine, A. F., & McPhaden, M. J. :How the July 2014 easterly wind burst gave the 2015–2016 El Niño a head start, *Geophysical research letters*, *43*(12), 6503-6510, https://doi.org/10.1002/2016GL069204, 2016.

MacDonald, A. M., Bonsor, H. C., Dochartaigh, B. É. Ó., & Taylor, R. G. :Quantitative maps of groundwater resources in Africa, *Environmental Research Letters*, *7*(2), 024009, 2012.

Manatsa, D., Matarira, C. H., & Mukwada, G.: Relative impacts of ENSO and Indian Ocean dipole/zonal mode on east SADC rainfall, *International Journal of Climatology*, *31*(4), 558-577, 2011.

Marthews, T. R., Otto, F. E. L., Mitchell, D., Dadson, S. J., & Jones, R. G.: The 2014 drought in the Horn of Africa: Attribution of meteorological drivers? [in "Explaining Extremes of 2014 from a Climate Perspective"] *Bulletin of the American Meteorological Society*, *96*(12), S83-S88, 2015.

Mishra, V., & Cherkauer, K. A.: Retrospective droughts in the crop growing season: Implications to corn and soybean yield in the Midwestern United States, *Agricultural and Forest Meteorology*, *150*(7-8), 1030-1045, 2010.

Mitchell, D., AchutaRao, K., Allen, M., Bethke, I., Beyerle, U., Ciavarella, A., ... & Ingram, W. :Half a degree additional warming, prognosis and projected impacts (HAPPI): background and experimental design, *Geoscientific Model Development*, *10*(2), 571-583, https://doi.org/10.5194/gmd-10-571-2017, 2017.

Nicholson, S. E.: Climate and climatic variability of rainfall over eastern Africa, *Reviews of Geophysics*, *55*(3), 590-635, 2017.

Philip, S., Kew, S. F., Jan van Oldenborgh, G., Otto, F., O'Keefe, S., Haustein, K., ... & Singh, R. Attribution analysis of the Ethiopian drought of 2015, *Journal of Climate*, *31*(6), 2465-2486, 2018.

Preethi, B., Sabin, T. P., Adedoyin, J. A., & Ashok, K.: Impacts of the ENSO Modoki and other tropical Indo-Pacific climate-drivers on African rainfall, *Scientific reports*, *5*, 16653, 2015.

Ratnam, J. V., Behera, S. K., Masumoto, Y., & Yamagata, T. :Remote effects of El Niño and Modoki events on the austral summer precipitation of southern Africa, *Journal of Climate*, *27*(10), 3802-3815, 2014.

Reason, C. J. C., Allan, R. J., Lindesay, J. A., & Ansell, T. J. : ENSO and climatic signals across the Indian Ocean basin in the global context: Part I, Interannual composite patterns. *International Journal of Climatology*, *20*(11), 1285-1327,2000.

Reason, C. J. C. : Subtropical Indian Ocean SST dipole events and southern African rainfall, *Geophysical Research Letters*, *28*(11), 2225-2227,2001

Robeson, S. M. :Revisiting the recent California drought as an extreme value, *Geophysical Research Letters*, *42*(16), 6771-6779, 2015.

Rodell, M., Houser, P. R., Jambor, U. E. A., Gottschalck, J., Mitchell, K., Meng, C. J., ... & Entin, J. K. ;The global land data assimilation system, *Bulletin of the American Meteorological Society*, *85*(3), 381-394, 2004.

Ropelewski, C. F., & Halpert, M. S. : Global and regional scale precipitation patterns associated with the El Niño/Southern Oscillation. *Monthly weather review*, *115*(8), 1606-1626,1987.

SADC 2016a: SADC regional situation update on El Nino-induced drought, Issue 02, 12th Sepetember2016,https://www.sadc.int/files/9514/7403/9132/SADC_Regional_Situation_Update_No-2_16-09-2016.pdf accessed 30/12/17,2016.

SADC 2016b: SADC Regional Vulnerability Assessment and Analysis Synthesis Report, State of Food Insecurity and Vulnerability in the Southern African Development Community 66pp,2016.

Saji, N. H., Goswami, B. N., Vinayachandran, P. N., & Yamagata, T.: A dipole mode in the tropical Indian Ocean, *Nature*, *401*(6751), 360, doi:10.1038/43854, 1999.

Scanlon, B. R., Longuevergne, L. , and Long, D.: Ground referencing GRACE satellite estimates of groundwater storage changes in the California Central Valley, USA *Water Resour. Res*. 48 W04520,2012.

Scanlon B R *et al* 2018 Global models underestimate large decadal declining and rising water storage trends relative to GRACE satellite data. *Proc. Nat. Acad. Sci.* https://doi.org/10.1073/pnas.1704665115

Scanlon, B. R., Zhang, Z., Save, H., Sun, A. Y., Schmied, H. M., van Beek, L. P., ... & Longuevergne, L. : Global models underestimate large decadal declining and rising water storage trends relative to GRACE satellite data, *Proceedings of the National Academy of Sciences*, 201704665, https://doi.org/10.1073/pnas.1704665115,2018.

Schneider U, Becker A, Finger P, Meyer-Christoffer A, Rudolf B, Ziese M 2011b GPCC Monitoring Product Version 4.0 at 1.0°: near real-time monthly land-surface precipitation from rain-gauges based on SYNOP and CLIMAT Data. doi: 10.5676/ DWD_GPCC/MP_M_V4_100

Schneider, U., Becker, A., Finger, P., Meyer-Christoffer, A., Ziese, M., & Rudolf, B. : GPCC's new land surface precipitation climatology based on quality-controlled in situ data and its role in quantifying the global water cycle, *Theoretical and Applied Climatology*, *115*(1-2), 15-40, 2014.

Shamsudduha M, Taylor R G and Longuevergne L 2012 Monitoring groundwater storage changes in the highly seasonal humid tropics: validation of GRACE measurements in the Bengal Basin *Water Resour. Res*. 48 W02508

Shamsudduha, M., Taylor, R. G., & Longuevergne, L.: Monitoring groundwater storage changes in the highly seasonal humid tropics: Validation of GRACE measurements in the Bengal Basin, *Water Resources Research*, *48*(2), 2012.

Shamsudduha, M., Taylor, R. G., Jones, D., Longuevergne, L., Owor, M., & Tindimugaya, C. :Recent changes in terrestrial water storage in the Upper Nile Basin: an evaluation of commonly used gridded GRACE products, *Hydrology and Earth system sciences*, *21*(9), 4533-4549, https://doi.org/10.5194/hess-21-4533-2017,2017.

Siderius, C., Gannon, K. E., Ndiyoi, M., Opere, A., Batisani, N., Olago, D., ... & Conway, D. :Hydrological response and complex impact pathways of the 2015/2016 El Niño in Eastern and Southern Africa, *Earth's Future*, *6*(1), doi:10.1002/2017EF000680,2-22, 2018.

Smith, T. M., Reynolds, R. W., Peterson, T. C., & Lawrimore, J. : Improvements to NOAA's historical merged land–ocean surface temperature analysis (1880–2006). *Journal of Climate*, *21*(10), 2283-2296,2008.

Stott, P. A., Hegerl, G. C., Herring, S. C., Hoerling, M .P., Peterson, T. C., Zhang, X., and Zwiers, F. W.: Introduction to explaining extreme events of 2013 from a climate perspective, *Bull. Amer. Meteor. Soc.* 95 S1–S3,2014

Swenson, S., & Wahr, J.: Post-processing removal of correlated errors in GRACE data, *Geophysical Research Letters*, *33*(8),2006.

Taylor, R. G., Todd, M. C., Kongola, L., Maurice, L., Nahozya, E., Sanga, H., & MacDonald, A. M. : Evidence of the dependence of groundwater resources on extreme rainfall in East Africa, *Nature Climate Change*, *3*(4), 374, 2013.

Vicente-Serrano, S. M., Beguería, S., & López-Moreno, J. I. : A multiscalar drought index sensitive to global warming: the standardized precipitation evapotranspiration index, *Journal of climate*, *23*(7), 1696-1718, 2010.

Watkins, M. M., Wiese, D. N., Yuan, D. N., Boening, C., & Landerer, F. W. : Improved methods for observing Earth's time variable mass distribution with GRACE using spherical cap mascons, *Journal of Geophysical Research: Solid Earth*, *120*(4), 2648-2671,2015.

Wiese, D. N., Yuan, D-N., Boening, C., Landerer, F. W., and Watkins, M. M.: JPL GRACE Mascon Ocean, Ice, and Hydrology Equivalent Water Height JPL RL05M.1. Ver. 1 PO.DAAC CA USA,2015.

Wiese, D. N., Landerer, F. W., and Watkins, M. M.: Quantifying and reducing leakage errors in the JPL RL05M GRACE mascon solution, *Water Resour. Res.* 52 7490-7502,2016.